Geometry Control and Optical Tunability of Metal–Cuprous Oxide Core–Shell Nanoparticles

Li Zhang, Hao Jing, Geoffrey Boisvert, John Z. He, and Hui Wang*

Department of Chemistry and Biochemistry, University of South Carolina, 631 Sumter Street, Columbia, South Carolina 29208, United States

ABSTRACT Metal–semiconductor hybrid heteronanostructures may exhibit synergistically reinforced optical responses and significantly enhanced optical tunability that essentially arise from the unique nanoscale interactions between the metal and semiconductor components. Elaboration of multicomponent hybrid nanoparticles allows us to achieve optimized or diversified material functionalities through precise control over the dimension and morphology of the constituent building units, on one hand, and through engineering their relative geometrical arrangement and interfacial structures, on the other hand. Here we study the geometry-dependent optical characteristics of metal–cuprous oxide (Cu_2O) core–shell hybrid nanoparticles in great detail through combined experimental and theoretical efforts. We demonstrate that several important geometrical parameters, such as shell thickness, shell crystallinity, shell porosity, and core composition, of the hybrid nanoparticles can be tailored in a highly precise and controllable manner through robust wet chemistry approaches. The tight control over the particle geometries provides unique opportunities for us to develop quantitative understanding of how the dimensions, morphologies, and electronic properties of the semiconducting shells and the geometry and compositions of the metallic cores affect the plasmon resonance frequencies, the light scattering and absorption cross sections, and the overall extinction spectral line shapes of the hybrid nanoparticles. Mie scattering theory calculations provide further insights into the origin of the geometrically tunable optical responses and the interesting extinction spectral line shapes of the hybrid nanoparticles that we have experimentally observed.

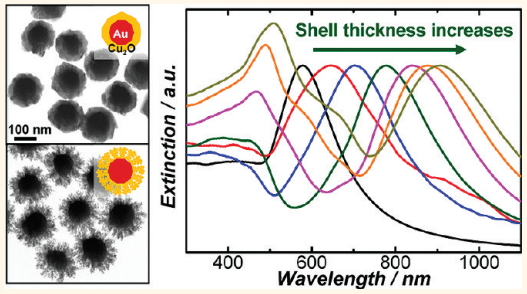

KEYWORDS: hybrid nanoparticles · heteronanostructures · metal · semiconductor · core–shell · plasmon resonance · geometry control · optical tunability

Metal–semiconductor heteronanostructures that combine multiple metallic and semiconducting components in one hybrid nanoscale entity have emerged as a new class of multifunctional subwavelength optical components with synergistically reinforced optical features, enhanced optical tunability, and even new characteristics that are otherwise inaccessible in any of the isolated components or their physical mixture counterparts.[1] Nanoscale interactions between the metallic and semiconducting domains inside a hybrid heteronanostructure may give rise to a series of interesting optical phenomena, such as altered photoluminescence quantum yields,[2–6] shifted plasmon resonance frequencies,[3,7,8] modified charge-carrier separation and recombination dynamics,[9–14] and the emergence of Fano-type spectral line shapes due to strong plasmon–exciton coupling effects.[15–17] The synergistic optical properties of the hybrid heteronanostructures are not only determined by the nature of each constituent component but also, in many cases, more sensitively dependent upon the geometrical arrangement of the building units.[1] Detailed, quantitative understanding of the geometry-optical property relationships of hybrid heteronanostructures provides the keystone for the rational design of hybrid nanoparticle systems with desired optical properties for widespread applications ranging from photovoltaics and photocatalysis to molecular imaging and spectroscopies.

Noble metals and cuprous oxide (Cu_2O) represent an interesting combination of materials for the construction of multifunctional metal–semiconductor hybrid heteronanostructures. Nanoparticles of noble metals exhibit plasmon-dominated optical properties that are sensitively dependent on their geometrical parameters.[18–22] By tailoring the particle geometry, one can fine-tune the optical responses of a metallic nanoparticle and set the plasmon resonances at a specific wavelength or spectral region to match a particular application. This has, in turn, stimulated tremendous interests in a rapidly expanding array of metallic nanostructures, such as nanorods,[23–28] nanorings,[29,30] nanoprisms,[31–35] nanostars,[36–38] nanoshells,[39–41] and nanocages,[42,43] with

* Address correspondence to wang344@mailbox.sc.edu.

Received for review February 6, 2012 and accepted March 23, 2012.

Published online March 24, 2012
10.1021/nn300546w

increased geometrical complexity and enriched plasmonic characteristics. As an interesting semiconducting material, Cu_2O may also exhibit interesting geometry-dependent optical tunability in various nanoparticle geometries. For example, it has been recently demonstrated that the Mie scattering and light absorption properties of Cu_2O nanoshells can be fine-tuned in the visible region by tailoring the dimensions and interior structures of the single-layer or multilayer nanoshells.[44,45] In contrast to more sophisticated nanostructures, spherical nanoparticles of noble metals exhibit rather limited plasmonic tuning range; however, as we recently demonstrated using Au–Cu_2O core–shell nanoparticles as a model system,[8] their plasmonic tunability may be greatly enriched and expanded by wrapping the metal nanoparticle inside a semiconducting nanoshell without changing the simple, spherically symmetric particle geometry. We have recently shown that by coating the surface of a Au nanoparticle with a polycrystalline Cu_2O shell composed of small nanoparticles, one can systematically shift the plasmon resonances of the Au core to longer wavelengths.[8] Such enhanced optical tunability essentially arises from the unique interactions between the metallic cores and semiconducting shells over the nanometer length scale.

Here we present a detailed, systematic study on the geometrically tunable optical properties of metal–Cu_2O core–shell nanoparticles through combined experimental and theoretical efforts. We have developed robust wet chemistry approaches through which a series of important geometrical parameters of the hybrid nanoparticles, such as shell thickness, shell crystallinity, shell porosity, and core compositions, can be tailored in a highly precise and controllable manner, allowing us to systematically fine-tune the particles' synergistic optical properties over the visible and near-infrared spectral regions. By correlating the experimental results with Mie scattering theory calculations, we have developed quantitative understanding of how the interactions between the core and the shell give rise to the highly tunable plasmon resonance frequencies and interesting extinction spectral line shapes of the hybrid nanoparticles. First, we demonstrate that hybrid nanoparticles with a Au core and a dense Cu_2O shell composed of single-crystalline domains can be fabricated through controllable epitaxial growth of Cu_2O on the surfaces of multi-twinned, quasi-spherical Au nanoparticles. The tight control over the shell thickness, coupled with Mie scattering theory calculations, allows us to gain physical insights into how the thickness and the electronic properties of the semiconducting shell profoundly impact the plasmon resonance frequencies, extinction spectral line shapes, and optical cross sections of the hybrid nanoparticles at a great level of precision and detail. Then, we show that hybrid nanoparticles composed of a quasi-spherical Au core coated with a polycrystalline, porous Cu_2O nanoshell can be fabricated through seed-mediated hierarchical assembly of Cu_2O nanoparticles. The capability of controlling the apparent thickness and packing density of the porous Cu_2O nanoshells provides unique opportunities for us to study how the shell porosity introduces modifications to the local dielectric functions of the semiconducting shells and consequently affects the resulting optical tunability of the hybrid nanoparticles. Finally, we demonstrate that our Cu_2O shell growth approaches can be extended from Au–Cu_2O to other metal–Cu_2O interfaces, such as Ag–Cu_2O and Pd–Cu_2O, and thus can be employed to fabricate Au–Ag–Cu_2O and Au–Pd–Cu_2O concentric triple-layer hybrid nanoparticles. These triple-layer core–shell nanoparticles with a higher level of structural sophistication provide interesting systems for us to investigate how the variation of metallic core compositions affects the synergistic plasmonic signatures and tunability of the multi-shelled hybrid nanoparticles.

RESULTS AND DISCUSSION

Hybrid Nanoparticles Composed of Au Core and Cu_2O Dense Shell. We adopted an epitaxial shell growth approach through which a dense Cu_2O nanoshell composed of single-crystalline domains can be controllably fabricated surrounding quasi-spherical Au nanoparticle cores. Epitaxial growth is currently one of the most extensively used methods for the fabrication of heteronanostructures composed of multiple components with small crystalline lattice mismatches (<5%). The closely matched lattices between noble metals allow for the controllable fabrication of metallic core–shell nanostructures with various compositional combinations, such as Au–Ag,[46–49] Au–Cu,[50] Au–Pd,[47,51–55] Au–Pt,[56,57] Pt–Pd,[57–60] and Au–Pd–Pt multilayered particles,[61,62] through solution-phase epitaxial growth approaches. For metal and semiconductor pairs with relatively large lattice mismatches and/or significantly different crystalline structures, the direct epitaxial growth of monocrystalline semiconductor layers on metallic surfaces becomes challenging.[63] To overcome the obstacle of lattice-matching constraint, alternative non-epitaxial approaches have been recently developed to fabricate a series of metal–semiconductor core–shell nanoparticles.[2,3,63,64] For Au and Cu_2O, the great similarity in their crystalline structures (face-centered cubic crystals) and the relatively small lattice mismatch (4.5%) make it possible to epitaxially grow Cu_2O layers on the surface of Au nanoparticles without much lattice stress under appropriate conditions.[65–69]

Our approach to epitaxially grow dense Cu_2O shells over the surface of Au nanoparticles is based on the controllable reduction of Cu^{2+} at 0 °C under basic conditions using hydrazine as a mild reducing agent. As illustrated in the transmission electron microscopy (TEM) images shown in Figure 1A–D, this approach

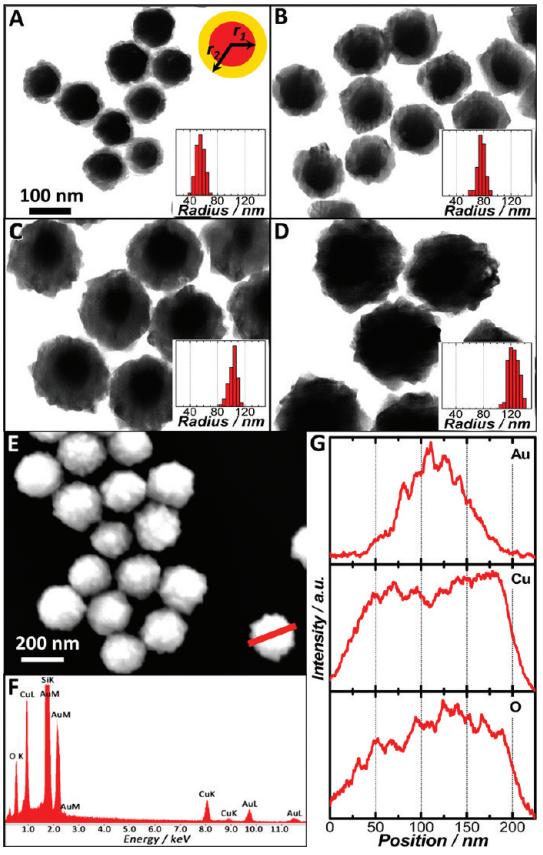

Figure 1. Structural characterizations of Au−Cu_2O core−shell nanoparticles with dense Cu_2O shells. TEM images of Au−Cu_2O particles with average core radius (r_1) of 49 nm and various average overall particle radii (r_2) of (A) 55, (B) 76, (C) 102, and (D) 124 nm. The upper-right inset of panel A shows the scheme of the cross section of one Au−Cu_2O core−shell nanoparticle. The bottom-right insets are histograms showing the particle size distribution for each sample. All of the TEM images share the same scale bar in panel A. (E) SEM image of Au−Cu_2O nanoparticles with average [r_1, r_2] = [49, 102] nm. (F) Integrated EDS spectrum obtained from one individual particle. (G) Spatial elemental distribution obtained from the EDS line scan measurements along the red line shown in panel E based on the L-lines of Au and K-lines of Cu and O.

allows us to precisely control the shell thickness over a broad size range from a few nanometers to over 100 nm by simply adjusting the molar ratio between the copper precursors and Au cores. The quasi-spherical shape of the Au cores (average radius of 49 nm; see a representative TEM image in Figure S1 in Supporting Information) is found to be well-preserved in the as-fabricated core−shell nanoparticles. The insets in Figure 1A−D show the histograms of overall particle radii obtained by analyzing more than 200 nanoparticles in the TEM images for each sample using Scion Image Software (version 4.0.3.2., Scion Corporation). The narrow single Gaussian distributions exhibited in these histograms indicate that the samples are highly monodisperse with narrow size distributions typically within 8% standard deviation.

The TEM images also reveal that the outer surfaces of the core−shell nanoparticles exhibit nanoscale textured features rather than being smooth, which can be further confirmed by the scanning electron microscopy (SEM) image shown in Figure 1E. It is apparent that nanoscale protrusions are distributed all over the outer surfaces of the particles and the particle surface becomes increasingly textured as the shell thickness progressively increases. Although the Au cores are generally regarded as quasi-spherical particles, they should be more accurately described as multi-twinned polyhedrons. The exposed outer surfaces of these Au quasi-spheres essentially consist of small but atomically well-defined crystalline facets with various orientations, each of which may serve as the substrate for the epitaxial growth of a Cu_2O layer. Epitaxial growth of Cu_2O on each Au facet would give rise to the formation of single-crystalline Cu_2O domains that would coalesce with each other to form a continuous dense shell surrounding the Au core. Since the epitaxially grown single-crystalline domains may have different orientations, the outer surface of the core−shell nanostructures obtained through such epitaxial overgrowth processes is expected to be textured with nanoscale protrusions rather than being a spherically nanocurved smooth surface. The selected area electron diffraction (SAED) pattern obtained from a single core−shell nanoparticle shown in Figure S2 in Supporting Information clearly indicates that the Cu_2O shell is essentially composed of a few single-crystalline domains with different orientations. We have also performed energy-dispersive X-ray spectroscopy (EDS) measurements (see Figure 1F) on individual particles to characterize the chemical composition of each nanoparticle, and the results of element analysis based on EDS line scans (Figure 1G) further verify the well-defined Au core/Cu_2O shell heterostructures of the hybrid nanoparticles.

The tight control over the shell thickness allows us to fine-tune the synergistic optical properties of core−shell hybrid nanoparticles over a broad spectral range. Figure 2A shows experimentally measured optical extinction (absorption + scattering) spectra of Au nanoparticles (bottom) and a series of Au−Cu_2O core−shell nanoparticles with increasing overall particle sizes (form bottom to top). The extinction spectrum of Au cores shows only one well-defined peak at 578 nm, which is the characteristic spectral feature of the dipole plasmon resonance of Au nanoparticles. For Au−Cu_2O core−shell nanoparticles, their plasmon resonance bands are observed to be red-shifted from 578 nm to longer wavelengths all the way deep into the near-infrared as the shell thickness progressively increases, while additional spectral features also gradually develop on the blue side of 600 nm in the visible, which can be assigned to the geometry-dependent optical characteristics of Cu_2O nanoshells as discussed in detail in previous publications.[8,44,69]

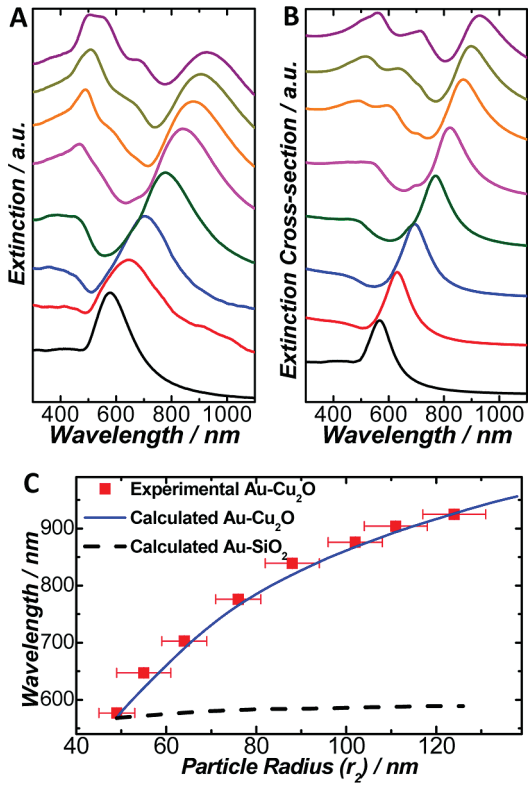

Figure 2. (A) Experimentally measured extinction spectra of Au nanoparticles (49 nm average radius, bottom curve) and Au−Cu_2O core−shell nanoparticles with average r_1 of 49 nm and various r_2 of 55, 64, 76, 88, 102, 111, and 124 nm (from bottom to top). (B) Calculated extinction spectra of individual Au−Cu_2O core−shell nanoparticles with [r_1, r_2] = [49, 49] nm, [49, 55] nm, [49, 64] nm, [49, 76] nm, [49, 88] nm, [49, 102] nm, [49, 111] nm, and [49, 124] nm (from bottom to top). Spectra are offset for clarity. (C) Experimentally measured and calculated plasmon resonance wavelength as a function of the overall radius of the Au−Cu_2O core−shell nanoparticles. The error bars for the experimental data points show the standard deviation determined by TEM measurements over 100 particles for each sample. The plots of calculated plasmon resonance wavelength as a function of the overall radius of Au−SiO_2 core−shell nanoparticles (r_1 = 49 nm) are also shown for comparison.

We used Mie scattering theory (applied to spherically concentric, multilayer nanoparticles)[45,70,71] to calculate the extinction spectra of individual, spherically symmetric Au−Cu_2O core−shell nanoparticles with fixed core radius of 49 nm and varying shell thickness that matches the experimentally fabricated nanoparticles. We employed the wavelength-dependent empirical dielectric functions of bulk Au[72] and Cu_2O[73] in these calculations, and the dielectric medium surrounding the particles was water with constant permittivity of 1.77. Both the peak positions and overall spectral line shapes of the calculated extinction spectra are in very good agreement with the experimental spectra, as shown in Figures 2B,C, which strongly indicates the validity and accuracy of using the current theoretical model to calculate the optical properties of the particles. In comparison to the theoretically calculated spectra, the near-infrared plasmon bands in experimental spectra are slightly dampened most likely due to the nanoscale surface roughness of the particles.[74,75]

As discussed in our previous paper,[8] the large red shift of the dipole plasmon resonance is essentially due to the large permittivity of Cu_2O ($\varepsilon \sim 7$) across the visible and near-infrared regions. In striking contrast to Au−Cu_2O core−shell nanoparticles, Au−SiO_2 core−shell nanoparticles display rather limited plasmonic tunability essentially because of the much smaller permittivity of SiO_2 ($\varepsilon = 2.04$).[69] Although excellent control over the core and shell dimensions of Au−SiO_2 and Ag−SiO_2 nanoparticles has been achieved experimentally, the plasmon resonance can only be shifted over limited spectral ranges as the SiO_2 shell thickness varies,[76−79] which is in agreement with the results of our Mie scattering theory calculations (dashed curve in Figure 2C).

Effects of Dielectric Properties of Cu_2O on the Optical Properties of Au−Cu_2O Hybrid Nanoparticles. The great plasmonic tunability observed in these Au−Cu_2O hybrid nanoparticles is not only determined by the core and shell dimensions but also directly related to the unique dielectric properties of Cu_2O. Cu_2O is an interesting semiconducting material with a bulk band gap value of ~2.17 eV. The wavelength-dependent empirical dielectric functions of bulk Cu_2O[73] are shown in Figure S3 in Supporting Information. In the visible region at wavelength range below ~600 nm, both the real part and imaginary part of Cu_2O's permittivity change dramatically as wavelength varies due to the strong excitonic interband transitions. Below the band gap energy (wavelengths longer than ~600 nm), however, Cu_2O is optically a dielectric material with the real part of permittivity around 7 and the imaginary part of permittivity close to 0. To quantitatively and completely understand how the electronic properties of the semiconducting Cu_2O nanoshell affect the synergistic optical properties of the Au−Cu_2O hybrid nanoparticles, we need to take both the real part and imaginary part of Cu_2O's dielectric functions into consideration.

In Figure 3A−C, we compare the calculated extinction spectra of Au−Cu_2O, Au−SiO_2, and Au−PbS core−shell nanoparticles. In comparison to the Au−SiO_2 particle, a Au−Cu_2O particle with exactly the same core−shell dimensions exhibits significantly further red-shifted plasmon resonances and enhanced extinction cross sections at the plasmon resonance wavelengths.[69] Since the plasmon resonance is shifted into the near-infrared beyond the spectral region where strong interband transitions of Cu_2O occur, the plasmon resonance frequencies and line shapes are primarily determined by the real part of the permittivity of Cu_2O with rather limited contributions from the small but nonzero imaginary part of the permittivity. In striking contrast to Au−Cu_2O, the plasmon resonance of Au−PbS core−shell nanoparticles occurs within the

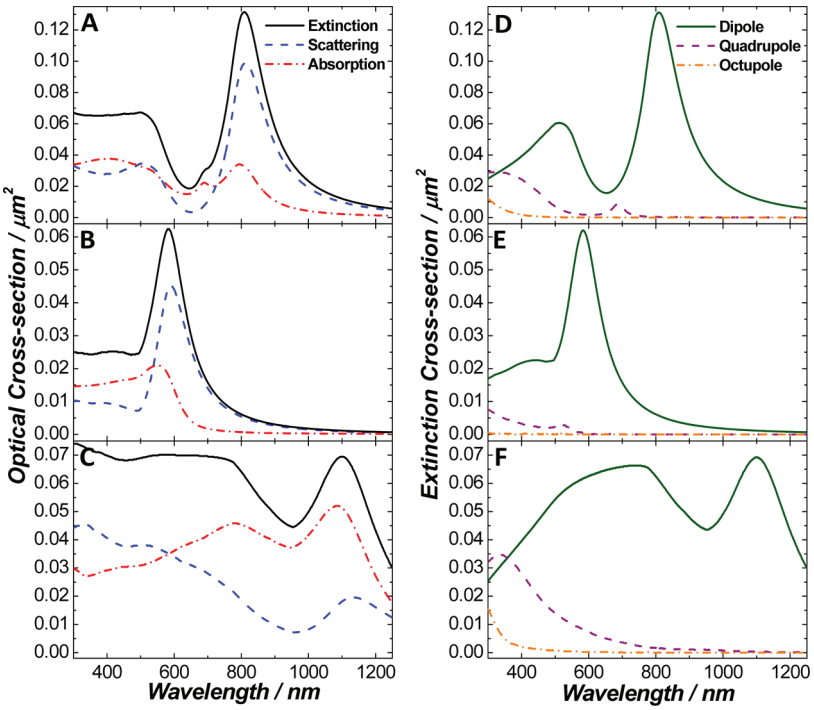

Figure 3. Calculated absorption, scattering, and extinction spectra of a core–shell nanoparticle with [r_1, r_2] = [49, 85] nm composed of (A) Au core and Cu_2O shell, (B) Au core and SiO_2 shell, and (C) Au core and PbS shell. The dielectric medium surrounding the outer surface of the particles is assumed to be H_2O. The calculated absorption, scattering, and extinction include 10 multipolar terms. Calculated dipole, quadrupole, octupole extinction spectra of a core–shell nanoparticle with [r_1, r_2] = [49, 85] nm composed of (D) Au core and Cu_2O shell, (E) Au core and SiO_2 shell, and (F) Au core and PbS shell.

spectral region above the band gap of the semiconducting PbS shell. As shown in Figure S4 in Supporting Information, PbS is a narrow band semiconductor with bulk band gap value of 0.37 eV, and both the real part and imaginary part of its permittivity are quite large throughout the whole near-infrared region.[73] A Au–PbS particle with the same set of geometrical parameters as Au–Cu_2O exhibits further red-shifted plasmon resonance simply because PbS has even larger real part of permittivity than Cu_2O. In contrast to Au–Cu_2O and Au–SiO_2 counterparts, strong damping of the plasmon resonance is observed with enhanced absorption and strongly dampened scattering due to the relatively large imaginary part of PbS's permittivity in the spectral range where plasmon resonance occurs. It is interesting that for the particle with core–shell dimensions under current considerations, their extinction spectra are all dominated by robust, sharp dipole plasmon resonances regardless of the dielectric properties of the shells (Figure 3D–F), whereas the optical extinctions of pure Au spherical particles in the similar overall size regime are more dominated by higher order multipole resonances with significantly broadened dipole plasmon resonances that are also red-shifted into the near-infrared (see Figure S5 in Supporting Information). The emergence of higher order multipole resonances and the broadening of the dipole resonance for Au particles in this mesoscopic size regime are essentially due to phase retardation effects.[80,81]

To develop a more quantitative understanding on how the real part of Cu_2O's permittivity affects the optical responses of Au–Cu_2O hybrid nanoparticles, we first neglect the effects of the finite imaginary part of permittivity by assuming a dielectric medium (constant, wavelength-independent real part of permittivity and zero imaginary part of the permittivity) surrounding the Au core. Figure 4A shows the calculated extinction spectra of a Au nanosphere (49 nm in radius) embedded in an infinitely large dielectric medium with varying permittivity. As the permittivity of the dielectric medium increases, the dipole plasmon resonance of the Au particle progressively red shifts and gets significantly broadened, while higher order multipole plasmon resonances, such as quadrupole and octupole, become increasingly pronounced. These phenomena can be well interpreted using the classical electromagnetic theory and have also been experimentally observed.[82] When the Au nanoparticle is wrapped inside a dielectric nanoshell with finite thickness, the dipole plasmon resonance shows similar red-shifting trend as the permittivity of the nanoshell progressively increases (see Figure 4B). However, the dipole plasmon resonance, which interacts strongly with the incident light, becomes very robust and dominates the overall extinction spectral line shape with only small contributions from quadrupole and other higher order multipole resonances. The spectral features that gradually develop in the visible region

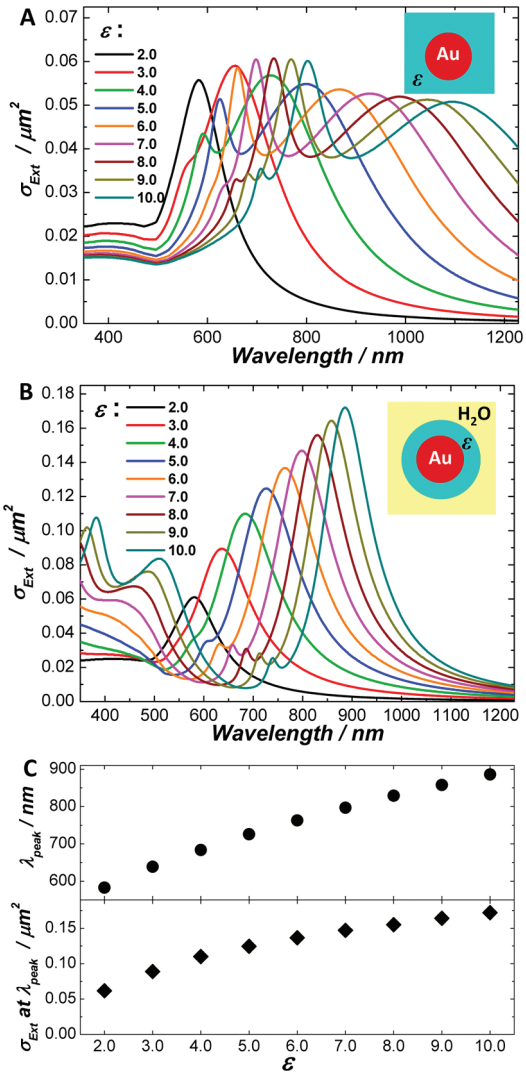

Figure 4. (A) Calculated extinction spectra of a Au nanosphere (49 nm in radius) dispersed in dielectric media with varying dielectric constants, ε. (B) Calculated extinction spectra of Au-dielectric core−shell nanoparticles composed of a 49 nm radius Au core and a 36 nm thick shell with varying ε. (C) Plots of dipole plasmon resonance wavelength (λ_{peak}) *vs* ε of the shell and plots of extinction cross section (σ_{Ext}) at λ_{peak} *vs* ε of the shell.

(below 600 nm) as shell permittivity increases can be assigned to the Mie scattering features from the dielectric nanoshells. Interestingly, there is also a progressive increase in dipole extinction cross sections as the permittivity of the nanoshell increases while the plasmon bandwidth remains almost the same. Dielectric shells with higher permittivities may give rise to increased imbalance of charges at the metal−dielectric interface upon plasmonic excitation, which may be the major reason for the enhancement of extinction cross sections. The evolution of dipole plasmon resonance wavelength and resonance extinction cross section as the shell permittivity varies is shown in detail in Figure 4C.

While the shift of plasmon resonances and the enhancement of extinction cross sections observed

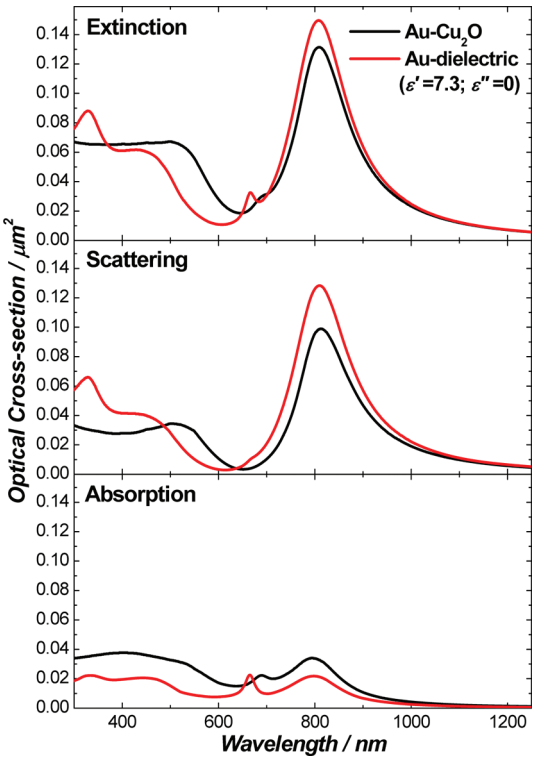

Figure 5. Calculated extinction (top panel), scattering (middle panel), and absorption (bottom panel) spectra of core−shell nanoparticles with [r_1, r_2] = [49, 85] nm composed of a Au core and a Cu_2O shell, and a Au core and a dielectric shell ($\varepsilon' = 7.3$, $\varepsilon'' = 0$).

in the Au−Cu_2O core−shell nanoparticles are primarily determined by the real part of Cu_2O's permittivity, the imaginary part of the permittivity of the semiconducting shells may further modulate the damping of plasmons, introducing interesting modifications to the absorption and scattering cross sections and consequently the overall extinction spectral line shapes. In Figure 5, we directly compare the calculated extinction, absorption, and scattering spectra of a Au−Cu_2O and a Au-dielectric core−shell nanoparticle with exactly the same core and shell radii. Assigning a constant permittivity of 7.3 to the dielectric shell would give essentially the same plasmon resonance frequency and bandwidth as those of the Au−Cu_2O hybrid particle except that the Au−Cu_2O nanoparticle has a smaller extinction cross section at the plasmon resonance wavelength than its Au-dielectric counterpart. The finite, nonzero imaginary part of shell permittivity plays non-negligible roles in modulating the damping of plasmons in the case of Au−Cu_2O core−shell nanoparticles. We have further decomposed the overall extinction into absorption and scattering. As shown in Figure 5B,C, the semiconducting Cu_2O nanoshell introduces a decrease in scattering cross section but an increase in absorption cross section at the plasmon resonance frequency in comparison to the Au-dielectric core−shell particle. Since the imaginary part of Cu_2O's permittivity is relatively small in the near-infrared, the effects of absorption enhancement and scattering

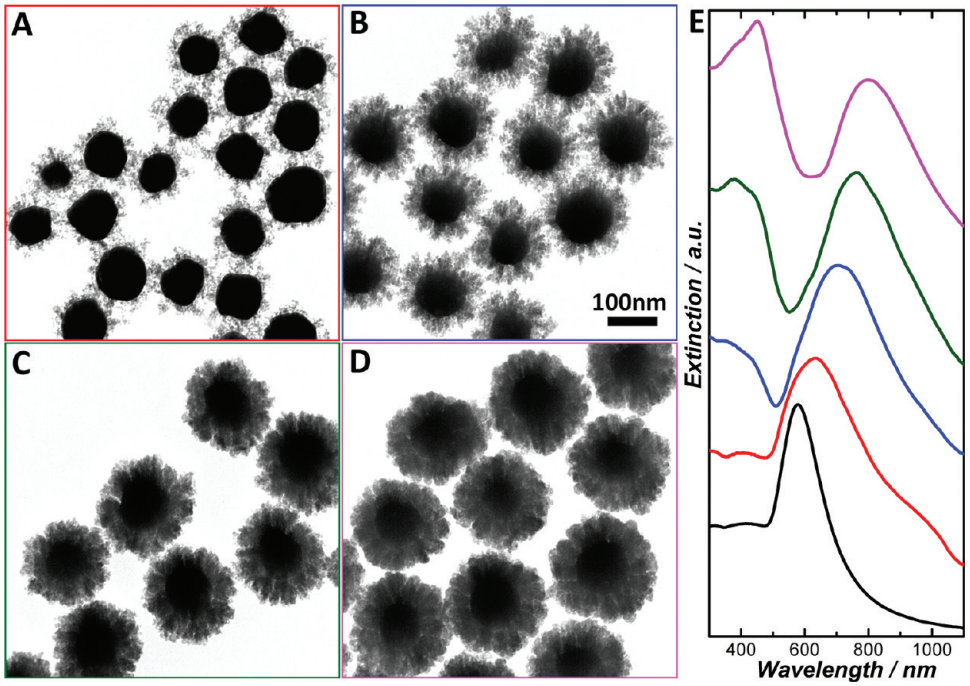

Figure 6. (A–D) TEM images of Au–Cu_2O core–shell nanoparticles with polycrystalline porous Cu_2O shells of various apparent thicknesses and packing densities. All TEM images share the same scale bar in panel B. (E) Experimentally measured extinction spectra of colloidal solutions of Au (bottom) and Au–Cu_2O nanoparticles with increasing apparent shell thickness and packing density (from bottom to top).

damping in Au–Cu_2O hybrid nanoparticles are not as significant as expected in Au–PbS core–shell nanoparticles. It is interesting that the plasmon damping of the quadrupole is more significant than the dipole resonance, making the overall extinction more dipolar in nature for the Au–Cu_2O particle than the Au-dielectric particle. This is largely due to the fact that quadrupole resonance occurs at wavelengths even closer to the spectral region where interband transitions of Cu_2O occur than the dipole resonance.

Hybrid Nanoparticles Composed of Au Core and Porous Cu_2O Shell. By changing the pH value and chemical compositions of the Cu_2O growth solution, the morphologies and crystalline structures of the resulting Cu_2O nanoshells can be significantly altered. We found that, at neutral pH, small Cu_2O nanocrystallites, typically 3–10 nm in size, would self-assemble surrounding a Au nanoparticle core to form a polycrystalline Cu_2O nanoshell with hierarchical porous structures in the presence of polyethylene glycol as a structural directing agent. The TEM images shown in Figure 6A–D clearly reveal that each Cu_2O shell is composed of a large number of small primary nanocrystals randomly oriented and hierarchically packed inside a porous shell framework. The polycrystalline nature of the Cu_2O shell and random orientation of the primary nanocrystals can be further confirmed by SAED measurements (see Figure S6 in Supporting Information). The hierarchical porous shell structures can also be visualized by SEM as shown in Figure S7 in Supporting Information. The EDS spectrum and line scan element analysis further verify the Au core, Cu_2O shell structure of the nanoparticles.

As shown in Figure 6A–D, both the apparent thickness and packing density of the Cu_2O nanoshells progressively increase as the molar ratio between copper precursors and Au seeds increases. Unlike the hybrid nanoparticles with dense Cu_2O shells, the plasmon resonance frequencies and extinction spectral line shapes of the hybrid nanoparticles with porous Cu_2O shells shown in Figure 6E are not only determined by the effective shell thickness but also related to the variation of the shell packing density. Decrease in the packing density or increase in the porosity of the Cu_2O shells leads to decrease in the effective local permittivity of the shells, resulting in plasmon resonance shift over narrower spectral ranges than the hybrid nanoparticles with the same core and shell dimensions but dense Cu_2O shell structures.

To accurately simulate the optical properties of nanoparticles with porous interior structures, effective permittivities which are related to the materials' packing densities should be used instead of the dielectric functions of bulk materials.[83] If we assume that the pores inside the Cu_2O shell are all filled with H_2O, then the wavelength-dependent real and imaginary parts of the effective dielectric functions of the porous shells can be obtained by weighing the bulk dielectric data of Cu_2O (ε_{Cu_2O}) and H_2O (ε_{H_2O}) based on the shell packing density (ρ) using the following equations:

$$\text{Real part}: \varepsilon'_{\text{effective}}(\lambda) = \rho\varepsilon'_{Cu_2O}(\lambda) + (1-\rho)\varepsilon'_{H_2O} = \rho\varepsilon'_{Cu_2O}(\lambda) + (1-\rho) \times 1.77 \quad (1)$$

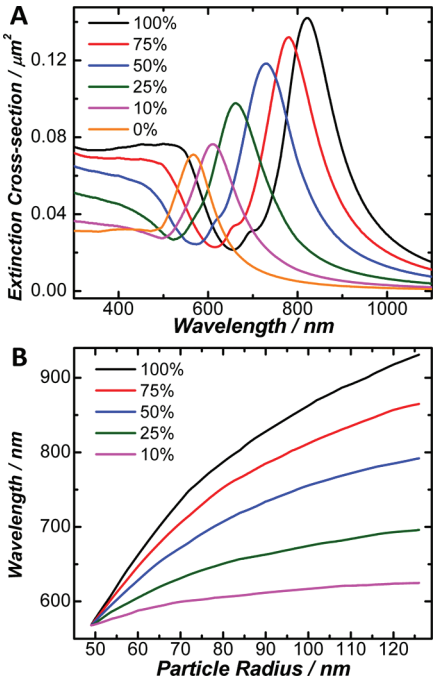

Figure 7. (A) Calculated extinction spectra of core–shell nanoparticles with a 49 nm Au core and a 41 nm thick shell with varying percentage of Cu_2O packing. (B) Shift of plasmon resonance wavelength as overall particle radius varies for Au–Cu_2O core–shell nanoparticles (49 nm radius Au core) with different shell packing density.

$$\text{Imaginary part}: \varepsilon''_{\text{effective}}(\lambda) = \rho\varepsilon''_{Cu_2O}(\lambda) + (1-\rho)\varepsilon''_{H_2O} = \rho\varepsilon''_{Cu_2O}(\lambda) \quad (2)$$

Figure 7A shows the calculated extinction spectra of a Au–Cu_2O core–shell nanoparticle (49 nm core radius and 41 nm shell thickness) with varying shell packing density, where 100% packing density corresponds to the dense Cu_2O shell and 0% packing density corresponds to the Au nanoparticle core dispersed in H_2O. As the shell packing density increases, the plasmon resonance progressively red shifts and the extinction cross section at the plasmon resonance wavelength also increases accordingly due to the increase in the effective shell permittivity. As shown in Figure 7B, the plasmon resonance frequencies of the core–shell nanoparticles become increasingly more sensitive to the shell thickness as the shell gets more densely packed. These indicate that, in addition to engineering the core radius and shell thickness, the optical properties of the Au–Cu_2O core–shell nanoparticles can be further fine-tuned by tailoring the porosity of the Cu_2O shells.

We can further construct geometrically more complicated Au–Cu_2O core–shell nanoparticles with multilayered shell structures. Using a stepwise epitaxial growth and hierarchical assembly approach, we can first coat the Au cores with a layer of dense Cu_2O nanoshell and then initiate the growth of a second layer of porous Cu_2O shell on the outer surface of the Cu_2O dense shell. Figure S8A–D in Supporting Information shows a series of TEM images of multilayered hybrid nanoparticles composed of Au cores, dense Cu_2O inner shells, and porous Cu_2O outer shells whose optical properties are also geometrically tunable, as shown in Figure S8E in Supporting Information.

Au–Ag–Cu_2O and Au–Pd–Cu_2O Triple-Layer Hybrid Nanoparticles. We have extended the Cu_2O shell growth approaches from Au–Cu_2O to other metal–Cu_2O interfaces, such as Ag–Cu_2O and Pd–Cu_2O, to controllably fabricate Au–Ag–Cu_2O and Au–Pd–Cu_2O concentric triple-layer hybrid nanoparticles. The optical properties of these multilayered particles are calculated by Mie scattering theory using the wavelength-dependent empirical dielectric functions of bulk Au,[72] Ag,[72] Pd,[84] and Cu_2O.[73] By replacing the monometallic Au cores with heterostructured bimetallic cores, further enhanced optical tunability and/or significantly enriched plasmonic features can be achieved in the triple-layer hybrid nanoparticles.

To fabricate Au–Ag–Cu_2O triple-layer nanoparticles, we first coated the surface of the Au nanoparticles with a thin but continuous layer of Ag to fabricate Au–Ag core–shell bimetallic nanoparticles. By controlling the amount ratio between the Au core and Ag precursors, the thickness of the Ag shells can be fine-controlled in the range from ~5 to ~40 nm with ~2 nm precision. Analogous to the fabrication of Au–Cu_2O nanoparticles, dense Cu_2O shells with controllable thicknesses can be epitaxially grown over the Ag surfaces subsequently to form Au–Ag–Cu_2O concentric triple-layer nanoparticles. Figure 8A shows an SEM image of the Au–Ag–Cu_2O nanoparticles with average geometrical parameters of $[R_1, R_2, R_3] = [49, 59, 91]$ nm. The EDS spectrum (Figure 8B) and line scan data (Figure 8C) clearly verify the Au–Ag–Cu_2O triple-layer core–shell structures of the particles. Figure 8D–G shows a series of TEM images of the Au–Ag core–shell bimetallic nanoparticles and Au–Ag–Cu_2O triple-layer particles with various Cu_2O shell thicknesses. The nanoscale textures on the outer surfaces of triple-layer particles can be clearly seen in both the SEM and TEM images.

Figure 8H shows the experimentally measured extinction spectra of Au–Ag bimetallic nanoparticles and Au–Ag–Cu_2O triple-layer nanoparticles with varying average Cu_2O shell thicknesses. The calculated extinction spectra of individual particles with the geometrical parameters that match the experimentally fabricated particles are shown accordingly in Figure 8I, which show very good agreement with the experimental spectra. As shown in Figure S9 in Supporting Information, we can further decompose the calculated extinctions into dipole, quadrupole, and octupole components for a Au–Ag core, a Cu_2O nanoshell, and a Au–Ag–Cu_2O triple-layer core–shell particle. Coating the surface of the Au nanoparticles with a thin layer of Ag not only increases the particle's extinction cross sections but also significantly

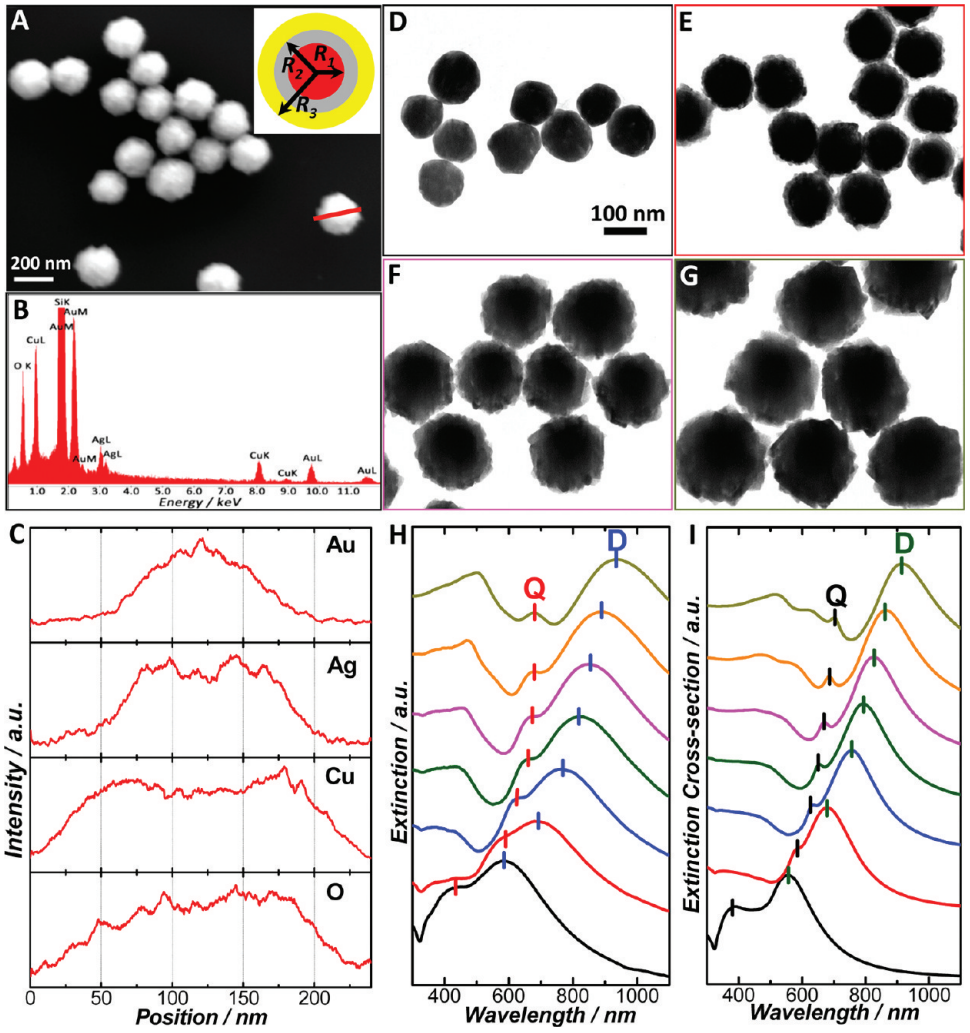

Figure 8. (A) SEM image of Au−Ag−Cu_2O triple-layer core−shell nanoparticles. The inset shows a schematic illustration of the triple-layer core−shell structure with a Au core, Ag inner shell, and Cu_2O outer shell. R_1, R_2, and R_3 represent the radii of the Au core, Au core + Ag shell, and Au core + Ag shell + Cu_2O shell, respectively. (B) Integrated EDS spectrum obtained from an individual particle. (C) Spatial elemental distribution obtained from the EDS line scan measurements along the red line shown in panel A, based on L-lines of Au and Ag and K-lines of Cu and O. (D) TEM images of Au−Ag core−shell nanoparticles with average R_1 of 49 nm and R_2 of 59 nm. TEM images of Au−Ag−Cu_2O triple-layer core−shell nanoparticles with average R_1 of 49 nm, R_2 of 59 nm, and various R_3 of (E) 70, (F) 91, and (G) 112 nm. All TEM images share the same scale bar in panel D. (H) Experimentally measured extinction spectra of Au−Ag core−shell and Au−Ag−Cu_2O triple-layer nanoparticles with average R_1 of 49 nm, R_2 of 59 nm, and various R_3 of 70, 79, 86, 91, 100, and 112 nm (from bottom to top). (I) Calculated extinction spectra of Au−Ag−Cu_2O triple-layer nanoparticles with [R_1, R_2, R_3] = [49, 59, 59] nm, [49, 59, 70] nm, [49, 59, 79] nm, [49, 59, 86] nm, [49, 59, 91] nm, [49, 59, 100] nm, and [49, 59, 112] nm (from bottom to top). The dipole and quadrupole features are labeled as D and Q, respectively, for both experimental and calculated data.

enriches the particle's plasmonic features as a well-defined quadrupole resonance band develops on the blue side of the dipole resonance in the extinction spectrum. The double-peaked spectral features observed here are the synergistic optical features of the bimetallic core−shell nanoparticles[85] and thus cannot be simply regarded as a linear combination of plasmon modes of the Au core and Ag shell, which is further verified by Mie scattering theory calculation results shown in Figure S10 in Supporting Information. The increased extinction cross sections and the emergence of strong quadrupole features observed in the Au−Ag core−shell nanoparticles are primarily a consequence of less plasmon damping due to the presence of Ag shells. The relative strengths of dipole, quadrupole, and even higher order multipole resonances can be further modulated through control over the thickness of the Ag shells without changing the size of the Au cores. As the Ag shell thickness increases, the higher order multipole plasmon resonances become significantly intensified with respect to the dipole resonance and the overall extinction spectral line shapes become increasingly dominated by the features of the Ag shells (see Figures S10, S11, and S12 in Supporting Information).

Upon the formation of Cu_2O nanoshells surrounding the Au−Ag core−shell nanoparticles, both the dipole and quadrupole resonances shift to significantly longer wavelengths into near-infrared in addition to

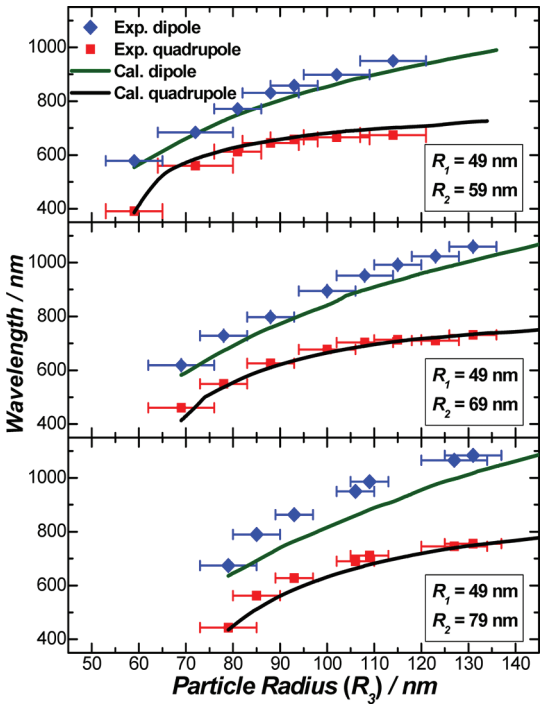

Figure 9. Shift of dipole and quadrupole plasmon resonance wavelengths of Au−Ag−Cu_2O triple-layer core−shell nanoparticles as the overall particle radius (R_3) varies for particles with various Au−Ag dimensions as indicated in each panel. The data points show the experimentally measured peak wavelengths, and the curves show the calculated values.

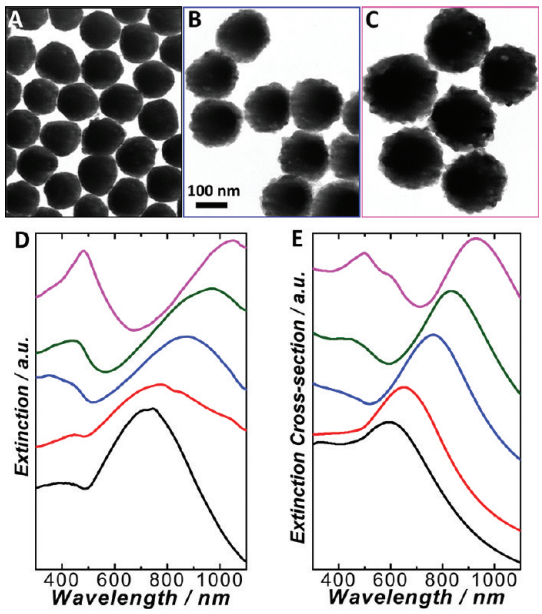

Figure 10. TEM images of (A) Au−Pd core−shell nanoparticles with average R_1 of 49 nm and R_2 of 65 nm, and Au−Pd−Cu_2O triple-layer nanoparticles with average R_1 of 49 nm, R_2 of 65 nm, and various R_3 of (B) 83 nm and (C) 107 nm. All TEM images show same scale bar in panel B. (D) Experimentally measured extinction spectra of Au−Pd core−shell and Au−Pd−Cu_2O triple-layer nanoparticles with average R_1 of 49 nm, R_2 of 65 nm, and various R_3 of 70, 83, 92, and 107 nm (from bottom to top). (E) Calculated extinction spectra of Au−Pd core−shell and Au−Pd−Cu_2O triple-layer nanoparticles with [R_1, R_2, R_3] = [49, 65, 65] nm, [49, 65, 70] nm, [49, 65, 83] nm, [49, 65, 92] nm, and [49, 65, 107] nm (from bottom to top).

the emergence of extinction features of the Cu_2O nanoshells in the visible. Figure 8H,I clearly shows that the extinction spectral shifts of both the dipole and quadrupole resonances are sensitively dependent on the thickness of the Cu_2O shells. The detailed correlations between the plasmon resonance wavelength and overall particle size, both experimentally measured and theoretically calculated, are shown in Figure 9 for both the dipole and quadrupole resonances of triple-layer nanoparticles with fixed Au core size and various Ag inner shell thicknesses. Similar to the Au−Cu_2O core−shell nanoparticles, hierarchical porous Cu_2O nanoshells with controllable packing densities and apparent thicknesses can also be fabricated surrounding the Au−Ag core−shell nanoparticles, and tunable optical characteristics can also be achieved through the geometry control of the particles as shown in Figure S13 in Supporting Information.

We have also used the same shell growth methods to synthesize Au−Pd−Cu_2O triple-layer hybrid nanoparticles with fine-controlled geometrical parameters. Figure 10A−C shows TEM images of Au−Pd−Cu_2O nanoparticles composed of 49 nm radius Au cores, 16 nm thick Pd inner shells, and dense Cu_2O outer shells with various thicknesses. The core−shell structures have been confirmed by EDS line scan measurements (Figure S14 in Supporting Information). As shown in Figure 10D,E, the plasmon resonance of the metallic cores is dampened with significantly weakened spectral features and broadened bandwidths upon the formation of Pd nanoshells, which is in agreement with previous observations.[51] Nevertheless, the geometry-dependent plasmon tunability of the Au−Pd−Cu_2O triple-layer nanoparticles is well-preserved. Both experimental observations and theoretical calculations clearly show that the plasmon resonances progressively red shift as the Cu_2O shell thickness increases. The experimental extinction spectra exhibit larger spectral shifts and broader bandwidths than the calculated spectra probably due to the structural nonideality and polydispersity of both the Pd inner shells and Cu_2O outer shells. In addition to dense Cu_2O shell structures, Au−Pd−Cu_2O triple-layer nanoparticles with polycrystalline, porous Cu_2O shells can also be fabricated following a similar protocol developed for Au−Cu_2O and Au−Ag−Cu_2O nanoparticles. The optical properties of these nanoparticles can be fine-tuned by tailoring the apparent thickness and packing density of the Cu_2O shells in a similar manner to the Au−Cu_2O and Au−Ag−Cu_2O nanoparticles (see Figure S15 in Supporting Information).

CONCLUSIONS

We have developed detailed, quantitative understanding of the geometry-dependent optical tunability

of metal−Cu_2O core−shell hybrid nanoparticles through combined experimental and theoretical efforts. We adopted an epitaxial shell growth approach through which hybrid nanoparticles with a quasi-spherical Au core and a dense Cu_2O nanoshell composed of single-crystalline domains can be controllably fabricated. The capability to tightly control the shell thickness provides unique opportunities for us to study, in great detail, how the variation of the shell thickness shifts the plasmon resonance frequencies and introduces interesting modification to the extinction spectral line shapes of the hybrid nanoparticles. We have performed Mie scattering theory calculations to theoretically interpret the origin of the geometrically tunable optical features of these hybrid nanoparticles. The large red shifts of plasmon resonances and significantly enhanced resonance extinction cross sections upon shell thickness increase are primarily due to the large real part of the permittivity of the Cu_2O shells, while the imaginary part of Cu_2O's permittivity also plays non-negligible roles in modulating the overall extinction spectral line shapes and the relative contributions of absorption and scattering to the overall extinction. We have also developed a self-assembly approach through which small Cu_2O nanocrystallites are hierarchically assembled into a polycrystalline, porous Cu_2O nanoshell surrounding a Au nanoparticle core. The plasmon resonance frequencies and extinction spectral line shapes of the hybrid nanoparticles with porous Cu_2O shells are not only determined by the apparent shell thickness but also related to the variation of the shell packing density. We have further extended the Cu_2O shell growth approaches from Au−Cu_2O to other metal−Cu_2O interfaces, such as Ag−Cu_2O and Pd−Cu_2O, to controllably fabricate Au−Ag−Cu_2O and Au−Pd−Cu_2O concentric triple-layer hybrid nanoparticles. These structurally more sophisticated triple-layer core−shell nanoparticles provide interesting systems for us to investigate how the variation of the core geometry and composition affects the synergistic optical characteristics of the multilayered hybrid heteronanostructures.

METHODS

All reagents were used as received without further purification. Ultrapure water (18.2 MΩ resistivity, Barnstead EasyPure II 7138) was used for all experiments. All of the reactions were carried out under constant magnetic stir with a speed of 300 rpm.

Synthesis of Au Nanoparticles. Au nanoparticles with average radius of ~49 nm, which were used as the core materials for core−shell nanoparticle fabrication, were synthesized by reducing chloroauric acid with formaldehyde at room temperature. The detailed procedure has been reported previously.[8] The final concentration of aqueous Au colloidal suspension was ~6×10^{10} particles/mL.

Synthesis of Au−Ag Core−Shell Nanoparticles. Au−Ag nanoparticles were synthesized by using the as-prepared Au nanoparticles as the seeds to mediate the Ag shell growth through reduction of Ag^+ with ascorbic acid. Briefly, 2 mL of Au colloidal solution was added into 60 mL of 1 wt % polyvinylpyrrolidone (PVP, average MW 58 000, Alfa Aesar) solution. Then various volumes (75−300 μL) of 0.1 M $AgNO_3$ (Alfa Aesar) and 300 μL of 0.5 M fresh-prepared ascorbic acid (Alfa Aesar) were added into the mixture under magnetic stir. The color of the solution changed from brick-red to beige in a few minutes, and the reaction mixture was kept stirring for 10 min. The Au−Ag nanoparticles were centrifuged (1500 rcf, 5 min), washed with 2 wt % of PVP solution twice, and finally redispersed in 5 mL of water (final concentration of ~2.4×10^{10} particles/mL).

Synthesis of Au−Pd Core−Shell Nanoparticles. Au−Pd core−shell nanoparticles can be fabricated through a Au nanoparticle-seeded Pd shell growth procedure. Au−Pd core−shell nanoparticles were fabricated following in a similar procedure for Au−Ag nanoparticle fabrication except that 1.5 mL of 0.01 M H_2PdCl_4 was introduced instead of 0.1 M $AgNO_3$. 0.01 M H_2PdCl_4 aqueous solution was prepared by dissolving 0.001 mol $PdCl_2$ (Sigma-Aldrich) in 100 mL of 0.02 M HCl (Fisher Scientific). The final color of the reaction solution was dark brown. Au−Pd core−shell nanoparticles were also washed and finally dispersed in 5 mL of water (final concentration of ~2.4×10^{10} particles/mL).

Synthesis of Metal−Cu_2O Core−Shell Nanoparticles. Metal−Cu_2O core−shell nanoparticles with either dense or porous shells were synthesized by reducing Cu^{2+} with hydrazine at selectively different pH values. For dense Cu_2O shells composed of single-crystalline domains, the core−shell nanoparticles were fabricated in basic solutions. Typically, a certain amount (80 μL for Au colloids and 200 μL for Au−Ag or Au−Pd colloids) of metal nanoparticles was first introduced into 5 mL of 2 wt % PVP aqueous solution. Varying amount (2.5−100 μL) of 0.1 M $Cu(NO_3)_2$ (Alfa Aesar) solution, depending on the desired thickness of the resulting Cu_2O shells, was subsequently added. The reaction mixtures were transferred into an ice bath, and then 11.2 μL of 5 M NaOH (Fisher Scientific) and 5 μL of $N_2H_4 \cdot 3H_2O$ solution (35 wt %, Sigma-Aldrich) were added under magnetic stir. The solutions were kept stirring for 10 min, and the nanoparticles were subsequently separated from the reaction solution by centrifugation (700 rcf, 5 min). For polycrystalline Cu_2O shells with hierarchical porosity, the shell growth was carried out at neutral pH (~7.2). In a typical procedure, a certain amount of colloidal metal seed solution (80 μL for Au and 200 μL for Au−Ag and Au−Pd) was added into 3 mL of 2 wt % poly(ethylene glycol)methyl ether (PEG, average MW 5000, Aldrich) aqueous solution, followed by the introduction of varying amount (5−50 μL) of 0.1 M $Cu(NO_3)_2$ and 35 wt % hydrazine solution (the molar ratio of Cu^{2+} to N_2H_4 was always kept at 2:7). The reaction mixture was stirred for 2 min. All metal−Cu_2O core−shell nanoparticles were washed with water and anhydrous ethanol and finally redispersed in ethanol.

Synthesis of Multilayer Nanoparticles Composed of Au Core, Dense Cu_2O Inner Shell, and Porous Cu_2O Outer Shell. A thin layer of polycrystalline, porous Cu_2O shell can be further grown on the outer surface of Au−Cu_2O core/dense shell nanoparticles to fabricate multilayer core−shell nanoparticles. Briefly, 480 μL of Au colloidal solution and 50 μL of 0.1 M $Cu(NO_3)_2$ solution were added into 30 mL of 2 wt % PVP solution under magnetic stir. The reaction mixture was transferred into an ice bath, and then 67.2 μL of 5 M NaOH and 30 μL of 35 wt % hydrazine solution were introduced. The solution was stirred for 10 min, and the resulting Au−Cu_2O nanoparticles were washed by water twice and redispersed in 900 μL of water. Then different amounts (5−15 μL) of 0.1 M $Cu(NO_3)_2$ and 160 μL of as-prepared Au−Cu_2O colloidal solution were introduced into 3 mL of 2 wt % PEG solution, followed by the introduction of varying amount of 35 wt % hydrazine solution (molar ratio of Cu^{2+} to N_2H_4 was fixed at 2:7). The reaction mixtures were kept stirring at room temperature for 2 min, and then the Au−Cu_2O multilayer core−shell nanoparticles were collected by centrifugation, washed with water and ethanol, and finally redispersed in ethanol for storage.

Characterizations. The morphologies and structures of the nanoparticles were characterized by TEM and SAED using a Hitachi H-8000 transmission electron microscope, which was operated at an accelerating voltage of 200 kV. All samples for TEM measurements were dispersed in ethanol and drop-dried on 200 mesh Formvar/carbon-coated Cu grids. The structures and compositions of the nanoparticles were also characterized by SEM and EDS measurements using a Zeiss Ultraplus thermal field emission scanning electron microscope. The samples for SEM and EDS measurements were dispersed in ethanol and drop-dried on silicon wafers. The optical extinction spectra of the nanoparticles were measured on aqueous colloidal suspensions at room temperature, using a Beckman Coulter Du 640 spectrophotometer.

Conflict of Interest: The authors declare no competing financial interest.

Acknowledgment. This work was supported by the Startup Funds provided by the College of Arts and Sciences of University of South Carolina. The authors would also like to acknowledge the USC Electron Microscopy Center for instrument use and scientific and technical assistance.

Supporting Information Available: Additional electron microscopy images, EDS results, experimentally measured optical extinction spectra, and calculated extinction spectra as noted in the text. This material is available free of charge *via* the Internet at http://pubs.acs.org.

REFERENCES AND NOTES

1. Costi, R.; Saunders, A. E.; Banin, U. Colloidal Hybrid Nanostructures: A New Type of Functional Materials. *Angew. Chem., Int. Ed.* **2010**, *49*, 4878–4897.
2. Chen, W. T.; Yang, T. T.; Hsu, Y. J. Au–CdS Core–Shell Nanocrystals with Controllable Shell Thickness and Photoinduced Charge Separation Property. *Chem. Mater.* **2008**, *20*, 7204–7206.
3. Li, M.; Yu, X. F.; Liang, S.; Peng, X. N.; Yang, Z. J.; Wang, Y. L.; Wang, Q. Q. Synthesis of Au–CdS Core–Shell Hetero-Nanorods with Efficient Exciton–Plasmon Interactions. *Adv. Funct. Mater.* **2011**, *21*, 1788–1794.
4. Liu, N. G.; Prall, B. S.; Klimov, V. I. Hybrid Gold/Silica/Nanocrystal-Quantum-Dot Superstructures: Synthesis and Analysis of Semiconductor–Metal Interactions. *J. Am. Chem. Soc.* **2006**, *128*, 15362–15363.
5. Mokari, T.; Rothenberg, E.; Popov, I.; Costi, R.; Banin, U. Selective Growth of Metal Tips onto Semiconductor Quantum Rods and Tetrapods. *Science* **2004**, *304*, 1787–1790.
6. Oh, E.; Hong, M. Y.; Lee, D.; Nam, S. H.; Yoon, H. C.; Kim, H. S. Inhibition Assay of Biomolecules Based on Fluorescence Resonance Energy Transfer (FRET) between Quantum Dots and Gold Nanoparticles. *J. Am. Chem. Soc.* **2005**, *127*, 3270–3271.
7. Lee, J. S.; Shevchenko, E. V.; Talapin, D. V. Au–PbS Core–Shell Nanocrystals: Plasmonic Absorption Enhancement and Electrical Doping *via* Intra-particle Charge Transfer. *J. Am. Chem. Soc.* **2008**, *130*, 9673–9675.
8. Zhang, L.; Blom, D. A.; Wang, H. Au–Cu_2O Core–Shell Nanoparticles: A Hybrid Metal–Semiconductor Heteronanostructure with Geometrically Tunable Optical Properties. *Chem. Mater.* **2011**, *23*, 4587–4598.
9. Costi, R.; Saunders, A. E.; Elmalem, E.; Salant, A.; Banin, U. Visible Light-Induced Charge Retention and Photocatalysis with Hybrid CdSe–Au Nanodumbbells. *Nano Lett.* **2008**, *8*, 637–641.
10. Dawson, A.; Kamat, P. V. Semiconductor–Metal Nanocomposites. Photoinduced Fusion and Photocatalysis of Gold-Capped TiO_2 (TiO_2/Gold) Nanoparticles. *J. Phys. Chem. B* **2001**, *105*, 960–966.
11. Formo, E.; Lee, E.; Campbell, D.; Xia, Y. N. Functionalization of Electrospun TiO_2 Nanofibers with Pt Nanoparticles and Nanowires for Catalytic Applications. *Nano Lett.* **2008**, *8*, 668–672.
12. Lee, J.; Hernandez, P.; Govorov, A. O.; Kotov, N. A. Exciton–Plasmon Interactions in Molecular Spring Assemblies of Nanowires and Wavelength-Based Protein Detection. *Nat. Mater.* **2007**, *6*, 291–295.
13. Li, P.; Wei, Z.; Wu, T.; Peng, Q.; Li, Y. D. Au–ZnO Hybrid Nanopyramids and Their Photocatalytic Properties. *J. Am. Chem. Soc.* **2011**, *133*, 5660–5663.
14. Linic, S.; Christopher, P.; Ingram, D. B. Plasmonic-Metal Nanostructures for Efficient Conversion of Solar to Chemical Energy. *Nat. Mater.* **2011**, *10*, 911–921.
15. Artuso, R. D.; Bryantt, G. W. Optical Response of Strongly Coupled Quantum Dot–Metal Nanoparticle Systems: Double Peaked Fano Structure and Bistability. *Nano Lett.* **2008**, *8*, 2106–2111.
16. Vasa, P.; Pomraenke, R.; Schwieger, S.; Mazur, Y. I.; Kunets, V.; Srinivasan, P.; Johnson, E.; Kihm, J. E.; Kim, D. S.; Runge, E.; *et al.* Coherent Exciton-Surface-Plasmon-Polariton Interaction in Hybrid Metal–Semiconductor Nanostructures. *Phys. Rev. Lett.* **2008**, *101*, 116801.
17. Yan, J. Y.; Zhang, W.; Duan, S. Q.; Zhao, X. G.; Govorov, A. O. Optical Properties of Coupled Metal–Semiconductor and Metal–Molecule Nanocrystal Complexes: Role of Multipole Effects. *Phys. Rev. B* **2008**, *77*, 165301.
18. Xia, Y. N.; Halas, N. J. Shape-Controlled Synthesis and Surface Plasmonic Properties of Metallic Nanostructures. *MRS Bull.* **2005**, *30*, 338–344.
19. Link, S.; El-Sayed, M. A. Optical Properties and Ultrafast Dynamics of Metallic Nanocrystals. *Annu. Rev. Phys. Chem.* **2003**, *54*, 331–366.
20. Jain, P. K.; Huang, X. H.; El-Sayed, I. H.; El-Sayed, M. A. Noble Metals on the Nanoscale: Optical and Photothermal Properties and Some Applications in Imaging, Sensing, Biology, and Medicine. *Acc. Chem. Res.* **2008**, *41*, 1578–1586.
21. El-Sayed, M. A. Some Interesting Properties of Metals Confined in Time and Nanometer Space of Different Shapes. *Acc. Chem. Res.* **2001**, *34*, 257–264.
22. Burda, C.; Chen, X. B.; Narayanan, R.; El-Sayed, M. A. Chemistry and Properties of Nanocrystals of Different Shapes. *Chem. Rev.* **2005**, *105*, 1025–1102.
23. Jana, N. R.; Gearheart, L.; Murphy, C. J. Wet Chemical Synthesis of Silver Nanorods and Nanowires of Controllable Aspect Ratio. *Chem. Commun.* **2001**, 617–618.
24. Link, S.; El-Sayed, M. A. Spectral Properties and Relaxation Dynamics of Surface Plasmon Electronic Oscillations in Gold and Silver Nanodots and Nanorods. *J. Phys. Chem. B* **1999**, *103*, 8410–8426.
25. Busbee, B. D.; Obare, S. O.; Murphy, C. J. An Improved Synthesis of High-Aspect-Ratio Gold Nanorods. *Adv. Mater.* **2003**, *15*, 414–416.
26. Murphy, C. J.; Jana, N. R. Controlling the Aspect Ratio of Inorganic Nanorods and Nanowires. *Adv. Mater.* **2002**, *14*, 80–82.
27. Murphy, C. J.; Sau, T. K.; Gole, A.; Orendorff, C. J. Surfactant-Directed Synthesis and Optical Properties of One-Dimensional Plasmonic Metallic Nanostructures. *MRS Bull.* **2005**, *30*, 349–355.
28. Nikoobakht, B.; El-Sayed, M. A. Preparation and Growth Mechanism of Gold Nanorods (NRs) Using Seed-Mediated Growth Method. *Chem. Mater.* **2003**, *15*, 1957–1962.
29. Aizpurua, J.; Hanarp, P.; Sutherland, D. S.; Kall, M.; Bryant, G. W.; de Abajo, F. J. G. Optical Properties of Gold Nanorings. *Phys. Rev. Lett.* **2003**, *90*, 057401.
30. Larsson, E. M.; Alegret, J.; Kall, M.; Sutherland, D. S. Sensing Characteristics of NIR Localized Surface Plasmon Resonances in Gold Nanorings for Application as Ultrasensitive Biosensors. *Nano Lett.* **2007**, *7*, 1256–1263.
31. Chen, S. H.; Carroll, D. L. Synthesis and Characterization of Truncated Triangular Silver Nanoplates. *Nano Lett.* **2002**, *2*, 1003–1007.
32. Jin, R. C.; Cao, Y. W.; Mirkin, C. A.; Kelly, K. L.; Schatz, G. C.; Zheng, J. G. Photoinduced Conversion of Silver Nanospheres to Nanoprisms. *Science* **2001**, *294*, 1901–1903.
33. Millstone, J. E.; Park, S.; Shuford, K. L.; Qin, L. D.; Schatz, G. C.; Mirkin, C. A. Observation of a Quadrupole Plasmon Mode for a Colloidal Solution of Gold Nanoprisms. *J. Am. Chem. Soc.* **2005**, *127*, 5312–5313.
34. Pastoriza-Santos, I.; Liz-Marzan, L. M. Synthesis of Silver Nanoprisms in DMF. *Nano Lett.* **2002**, *2*, 903–905.

35. Sun, Y. G.; Xia, Y. N. Triangular Nanoplates of Silver: Synthesis, Characterization, and Use as Sacrificial Templates for Generating Triangular Nanorings of Gold. *Adv. Mater.* **2003**, *15*, 695–699.
36. Hao, E.; Bailey, R. C.; Schatz, G. C.; Hupp, J. T.; Li, S. Y. Synthesis and Optical Properties of "Branched" Gold Nanocrystals. *Nano Lett.* **2004**, *4*, 327–330.
37. Kim, D. Y.; Yu, T.; Cho, E. C.; Ma, Y. Y.; Park, O. O.; Xia, Y. N. Synthesis of Gold Nano-hexapods with Controllable Arm Lengths and Their Tunable Optical Properties. *Angew. Chem., Int. Ed.* **2011**, *50*, 6328–6331.
38. Nehl, C. L.; Liao, H. W.; Hafner, J. H. Optical Properties of Star-Shaped Gold Nanoparticles. *Nano Lett.* **2006**, *6*, 683–688.
39. Oldenburg, S. J.; Averitt, R. D.; Westcott, S. L.; Halas, N. J. Nanoengineering of Optical Resonances. *Chem. Phys. Lett.* **1998**, *288*, 243–247.
40. Prodan, E.; Radloff, C.; Halas, N. J.; Nordlander, P. A Hybridization Model for the Plasmon Response of Complex Nanostructures. *Science* **2003**, *302*, 419–422.
41. Wang, H.; Brandl, D. W.; Nordlander, P.; Halas, N. J. Plasmonic Nanostructures: Artificial Molecules. *Acc. Chem. Res.* **2007**, *40*, 53–62.
42. Chen, J. Y.; McLellan, J. M.; Siekkinen, A.; Xiong, Y. J.; Li, Z. Y.; Xia, Y. N. Facile Synthesis of Gold–Silver Nanocages with Controllable Pores on the Surface. *J. Am. Chem. Soc.* **2006**, *128*, 14776–14777.
43. Chen, J. Y.; Wiley, B.; Li, Z. Y.; Campbell, D.; Saeki, F.; Cang, H.; Au, L.; Lee, J.; Li, X. D.; Xia, Y. N. Gold Nanocages: Engineering Their Structure for Biomedical Applications. *Adv. Mater.* **2005**, *17*, 2255–2261.
44. Zhang, L.; Wang, H. Cuprous Oxide Nanoshells with Geometrically Tunable Optical Properties. *ACS Nano* **2011**, *5*, 3257–3267.
45. Zhang, L.; Wang, H. Interior Structural Tailoring of Cu_2O Shell-in-Shell Nanostructures through Multistep Ostwald Ripening. *J. Phys. Chem. C* **2011**, *115*, 18479–18485.
46. Cho, E. C.; Camargo, P. H. C.; Xia, Y. N. Synthesis and Characterization of Noble-Metal Nanostructures Containing Gold Nanorods in the Center. *Adv. Mater.* **2010**, *22*, 744–748.
47. Fan, F. R.; Liu, D. Y.; Wu, Y. F.; Duan, S.; Xie, Z. X.; Jiang, Z. Y.; Tian, Z. Q. Epitaxial Growth of Heterogeneous Metal Nanocrystals: From Gold Nano-octahedra to Palladium and Silver Nanocubes. *J. Am. Chem. Soc.* **2008**, *130*, 6949–6951.
48. Park, G.; Seo, D.; Jung, J.; Ryu, S.; Song, H. Shape Evolution and Gram-Scale Synthesis of Gold@Silver Core–Shell Nanopolyhedrons. *J. Phys. Chem. C* **2011**, *115*, 9417–9423.
49. Sanchez-Iglesias, A.; Carbo-Argibay, E.; Glaria, A.; Rodriguez-Gonzalez, B.; Perez-Juste, J.; Pastoriza-Santos, I.; Liz-Marzan, L. M. Rapid Epitaxial Growth of Ag on Au Nanoparticles: From Au Nanorods to Core–Shell Au@Ag Octahedrons. *Chem.—Eur. J.* **2010**, *16*, 5558–5563.
50. Tsuji, M.; Yamaguchi, D.; Matsunaga, M.; Alam, M. J. Epitaxial Growth of Au@Cu Core–Shell Nanocrystals Prepared Using the PVP-Assisted Polyol Reduction Method. *Cryst. Growth Des.* **2010**, *10*, 5129–5135.
51. Hu, J. W.; Li, J. F.; Ren, B.; Wu, D. Y.; Sun, S. G.; Tian, Z. Q. Palladium-Coated Gold Nanoparticles with a Controlled Shell Thickness Used as Surface-Enhanced Raman Scattering Substrate. *J. Phys. Chem. C* **2007**, *111*, 1105–1112.
52. Lim, B.; Kobayashi, H.; Yu, T.; Wang, J. G.; Kim, M. J.; Li, Z. Y.; Rycenga, M.; Xia, Y. N. Synthesis of Pd–Au Bimetallic Nanocrystals *via* Controlled Overgrowth. *J. Am. Chem. Soc.* **2010**, *132*, 2506–2507.
53. Lu, C. L.; Prasad, K. S.; Wu, H. L.; Ho, J. A. A.; Huang, M. H. Au Nanocube-Directed Fabrication of Au–Pd Core–Shell Nanocrystals with Tetrahexahedral, Concave Octahedral, and Octahedral Structures and Their Electrocatalytic Activity. *J. Am. Chem. Soc.* **2010**, *132*, 14546–14553.
54. Wang, A. N.; Peng, Q.; Li, Y. D. Rod-Shaped Au–Pd Core–Shell Nanostructures. *Chem. Mater.* **2011**, *23*, 3217–3222.
55. Wang, F.; Sun, L. D.; Feng, W.; Chen, H. J.; Yeung, M. H.; Wang, J. F.; Yan, C. H. Heteroepitaxial Growth of Core–Shell and Core–Multishell Nanocrystals Composed of Palladium and Gold. *Small* **2010**, *6*, 2566–2575.
56. Feng, L. L.; Wu, X. C.; Ren, L. R.; Xiang, Y. J.; He, W. W.; Zhang, K.; Zhou, W. Y.; Xie, S. S. Well-Controlled Synthesis of Au@Pt Nanostructures by Gold-Nanorod-Seeded Growth. *Chem.—Eur. J.* **2008**, *14*, 9764–9771.
57. Habas, S. E.; Lee, H.; Radmilovic, V.; Somorjai, G. A.; Yang, P. Shaping Binary Metal Nanocrystals through Epitaxial Seeded Growth. *Nat. Mater.* **2007**, *6*, 692–697.
58. Jiang, M. J.; Lim, B.; Tao, J.; Camargo, P. H. C.; Ma, C.; Zhu, Y. M.; Xia, Y. N. Epitaxial Overgrowth of Platinum on Palladium Nanocrystals. *Nanoscale* **2010**, *2*, 2406–2411.
59. Lim, B.; Wang, J. G.; Camargo, P. H. C.; Jiang, M. J.; Kim, M. J.; Xia, Y. N. Facile Synthesis of Bimetallic Nanoplates Consisting of Pd Cores and Pt Shells through Seeded Epitaxial Growth. *Nano Lett.* **2008**, *8*, 2535–2540.
60. Zhang, H.; Jin, M. S.; Wang, J. G.; Kim, M. J.; Yang, D. R.; Xia, Y. N. Nanocrystals Composed of Alternating Shells of Pd and Pt Can Be Obtained by Sequentially Adding Different Precursors. *J. Am. Chem. Soc.* **2011**, *133*, 10422–10425.
61. Wang, L.; Yamauchi, Y. Autoprogrammed Synthesis of Triple-Layered Au@Pd@Pt Core–Shell Nanoparticles Consisting of a Au@Pd Bimetallic Core and Nanoporous Pt Shell. *J. Am. Chem. Soc.* **2010**, *132*, 13636–13638.
62. Wang, L.; Yamauchi, Y. Strategic Synthesis of Trimetallic Au@Pd@Pt Core–Shell Nanoparticles from Poly(vinylpyrrolidone)-Based Aqueous Solution toward Highly Active Electrocatalysts. *Chem. Mater.* **2011**, *23*, 2457–2465.
63. Zhang, J. T.; Tang, Y.; Lee, K.; Ouyang, M. Nonepitaxial Growth of Hybrid Core–Shell Nanostructures with Large Lattice Mismatches. *Science* **2010**, *327*, 1634–1638.
64. Sun, Z. H.; Yang, Z.; Zhou, J. H.; Yeung, M. H.; Ni, W. H.; Wu, H. K.; Wang, J. F. A General Approach to the Synthesis of Gold–Metal Sulfide Core–Shell and Heterostructures. *Angew. Chem., Int. Ed.* **2009**, *48*, 2881–2885.
65. Kuo, C. H.; Hua, T. E.; Huang, M. H. Au Nanocrystal-Directed Growth of Au–Cu_2O Core–Shell Heterostructures with Precise Morphological Control. *J. Am. Chem. Soc.* **2009**, *131*, 17871–17878.
66. Kuo, C. H.; Yang, Y. C.; Gwo, S.; Huang, M. H. Facet-Dependent and Au Nanocrystal-Enhanced Electrical and Photocatalytic Properties of Au–Cu_2O Core–Shell Heterostructures. *J. Am. Chem. Soc.* **2011**, *133*, 1052–1057.
67. Wang, W. C.; Lyu, L. M.; Huang, M. H. Investigation of the Effects of Polyhedral Gold Nanocrystal Morphology and Facets on the Formation of Au–Cu_2O Core–Shell Heterostructures. *Chem. Mater.* **2011**, *23*, 2677–2684.
68. Connell, J. G.; Al Balushi, Z. Y.; Sohn, K.; Huang, J. X.; Lauhon, L. J. Growth of Ge Nanowires from Au–Cu Alloy Nanoparticle Catalysts Synthesized from Aqueous Solution. *J. Phys. Chem. Lett.* **2010**, *1*, 3360–3365.
69. Liu, D. Y.; Ding, S. Y.; Lin, H. X.; Liu, B. J.; Ye, Z. Z.; Fan, F. R.; Ren, B.; Tian, Z. Q. Distinctive Enhanced and Tunable Plasmon Resonant Absorption from Controllable Au@Cu_2O Nanoparticles: Experimental and Theoretical Modeling. *J. Phys. Chem. C* **2012**, *116*, 4477–4483.
70. Aden, A. L.; Kerker, M. Scattering of Electromagnetic Waves from Two Concentric Spheres. *J. Appl. Phys.* **1951**, *22*, 1242–1246.
71. Radloff, C.; Halas, N. J. Plasmonic Properties of Concentric Nanoshells. *Nano Lett.* **2004**, *4*, 1323–1327.
72. Johnson, P. B.; Christy, R. W. Optical-Constants of Noble-Metals. *Phys. Rev. B* **1972**, *6*, 4370–4379.
73. Palik, E. D., Ed. *Handbook of Optical Constants of Solids*; Academic Press: San Diego, CA, 1991; Vol. 2.
74. Wang, H.; Goodrich, G. P.; Tam, F.; Oubre, C.; Nordlander, P.; Halas, N. J. Controlled Texturing Modifies the Surface Topography and Plasmonic Properties of Au Nanoshells. *J. Phys. Chem. B* **2005**, *109*, 11083–11087.
75. Wang, H.; Fu, K.; Drezek, R. A.; Halas, N. J. Light Scattering from Spherical Plasmonic Nanoantennas: Effects of Nanoscale Roughness. *Appl. Phys. B: Laser Opt.* **2006**, *84*, 191–195.
76. Lu, Y.; Yin, Y. D.; Li, Z. Y.; Xia, Y. A. Synthesis and Self-Assembly of Au@SiO_2 Core–Shell Colloids. *Nano Lett.* **2002**, *2*, 785–788.

77. Evanoff, D. D.; White, R. L.; Chumanov, G. Measuring the Distance Dependence of the Local Electromagnetic Field from Silver Nanoparticles. *J. Phys. Chem. B* **2004**, *108*, 1522–1524.
78. Salgueirino-Maceira, V.; Caruso, F.; Liz-Marzan, L. M. Coated Colloids with Tailored Optical Properties. *J. Phys. Chem. B* **2003**, *107*, 10990–10994.
79. Aslan, K.; Wu, M.; Lakowicz, J. R.; Geddes, C. D. Fluorescent Core−Shell Ag@SiO_2 Nanocomposites for Metal-Enhanced Fluorescence and Single Nanoparticle Sensing Platforms. *J. Am. Chem. Soc.* **2007**, *129*, 1524–1525.
80. Westcott, S. L.; Jackson, J. B.; Radloff, C.; Halas, N. J. Relative Contributions to the Plasmon Line Shape of Metal Nanoshells. *Phys. Rev. B* **2002**, *66*, 155431.
81. Wang, H.; Halas, N. J. Mesoscopic Au "Meatball" Particles. *Adv. Mater.* **2008**, *20*, 820–825.
82. Tam, F.; Moran, C.; Halas, N. J. Geometrical Parameters Controlling Sensitivity of Nanoshell Plasmon Resonances to Changes in Dielectric Environment. *J. Phys. Chem. B* **2004**, *108*, 17290–17294.
83. Bigall, N. C.; Hartling, T.; Klose, M.; Simon, P.; Eng, L. M.; Eychmuller, A. Monodisperse Platinum Nanospheres with Adjustable Diameters from 10 to 100 nm: Synthesis and Distinct Optical Properties. *Nano Lett.* **2008**, *8*, 4588–4592.
84. Johnson, P. B.; Christy, R. W. Optical-Constants of Transition-Metals: Ti, V, Cr, Mn, Fe, Co, Ni, and Pd. *Phys. Rev. B* **1974**, *9*, 5056–5070.
85. Chuntonov, L.; Bar-Sadan, M.; Houben, L.; Harant, G. Correlating Electron Tomography and Plasmon Spectroscopy of Single Noble Metal Core−Shell Nanoparticles. *Nano Lett.* **2012**, *12*, 145–150.